Supplementary Information

Sex-specific trajectories of nonlinear immune aging at single cell level

Harry Park[1,2,3], Nina Le Bert[4], Antonio Bertoletti[4], Nicholas Tolwinski[3], Jan Gruber[5,6,7] and Jacques Behmoaras[1,2*]

[1]Centre for Biomedical Data Science, Duke-NUS Medical School, Singapore, Singapore
[2]Program in Cardiovascular and Metabolic Disorders, Duke-NUS Medical School, Singapore
[3]Program in Cancer and Stem Cell Biology, Duke-NUS Medical School, Singapore, Singapore
[4]Program in Emerging Infectious Diseases, Duke-NUS Medical School, Singapore, Singapore
[5]Healthy Longevity Translational Research Program, Yong Loo Lin School of Medicine, National University of Singapore, Singapore, Singapore
[6]Center for Healthy Longevity, National University Health System, Singapore, Singapore
[7]Department of Biochemistry, Yong Loo Lin School of Medicine, National University of Singapore, Singapore, Singapore

Correspondence: jacquesb@duke-nus.edu.sg

This supplementary information file includes:

Supplementary Figures 1-19

Supplementary Tables 1-2

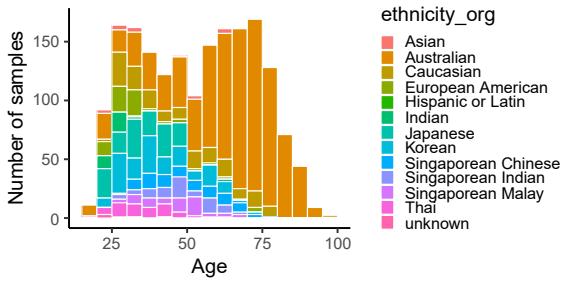

Supplementary Fig. 1: Age and self-reported ethnicity distribution of the four datasets combined. Age and self-reported ethnicity distribution of the four datasets combined (n = 1,828 donors).

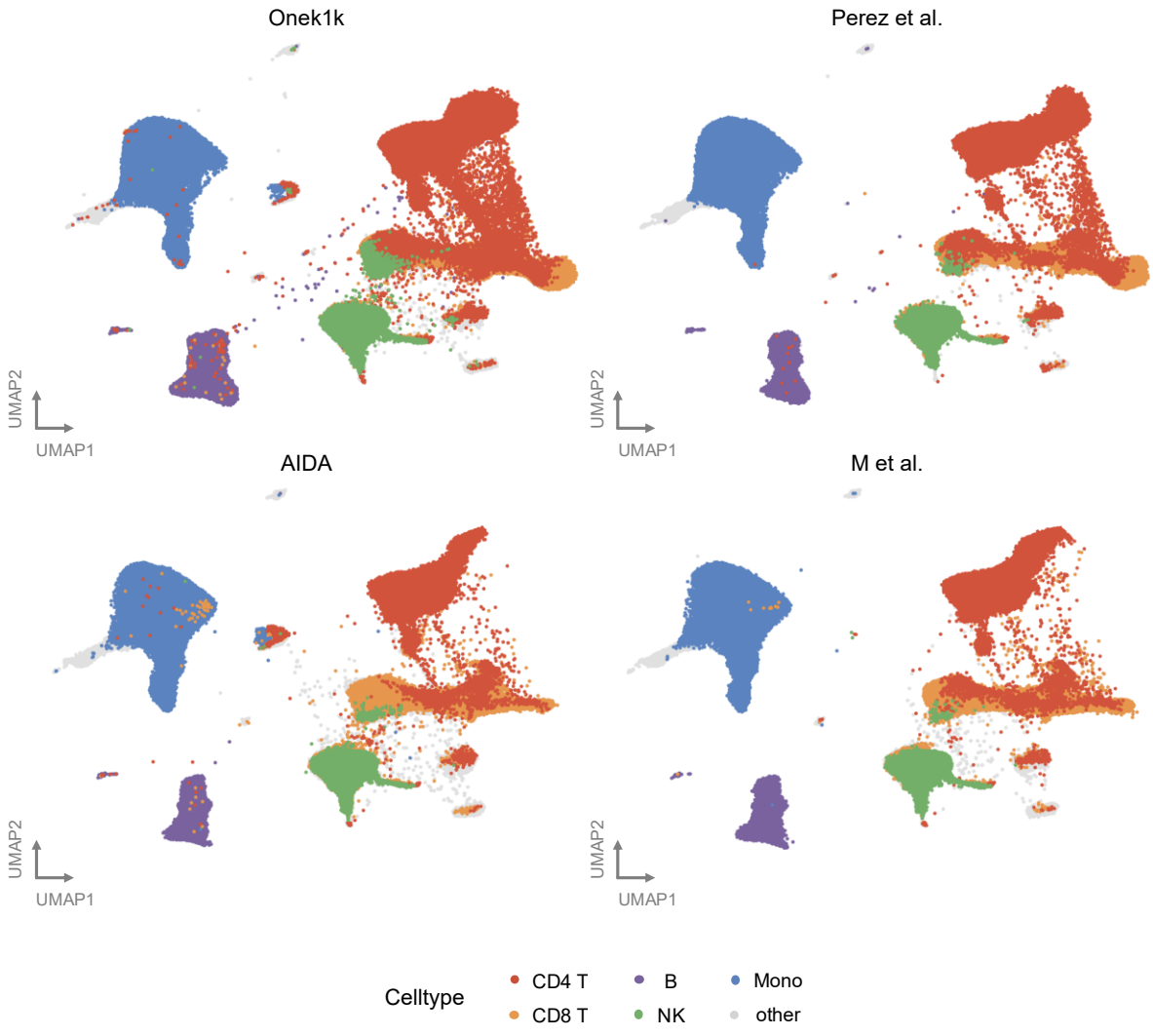

Supplementary Fig. 2: UMAP projection of major PBMC cell types across the four datasets.

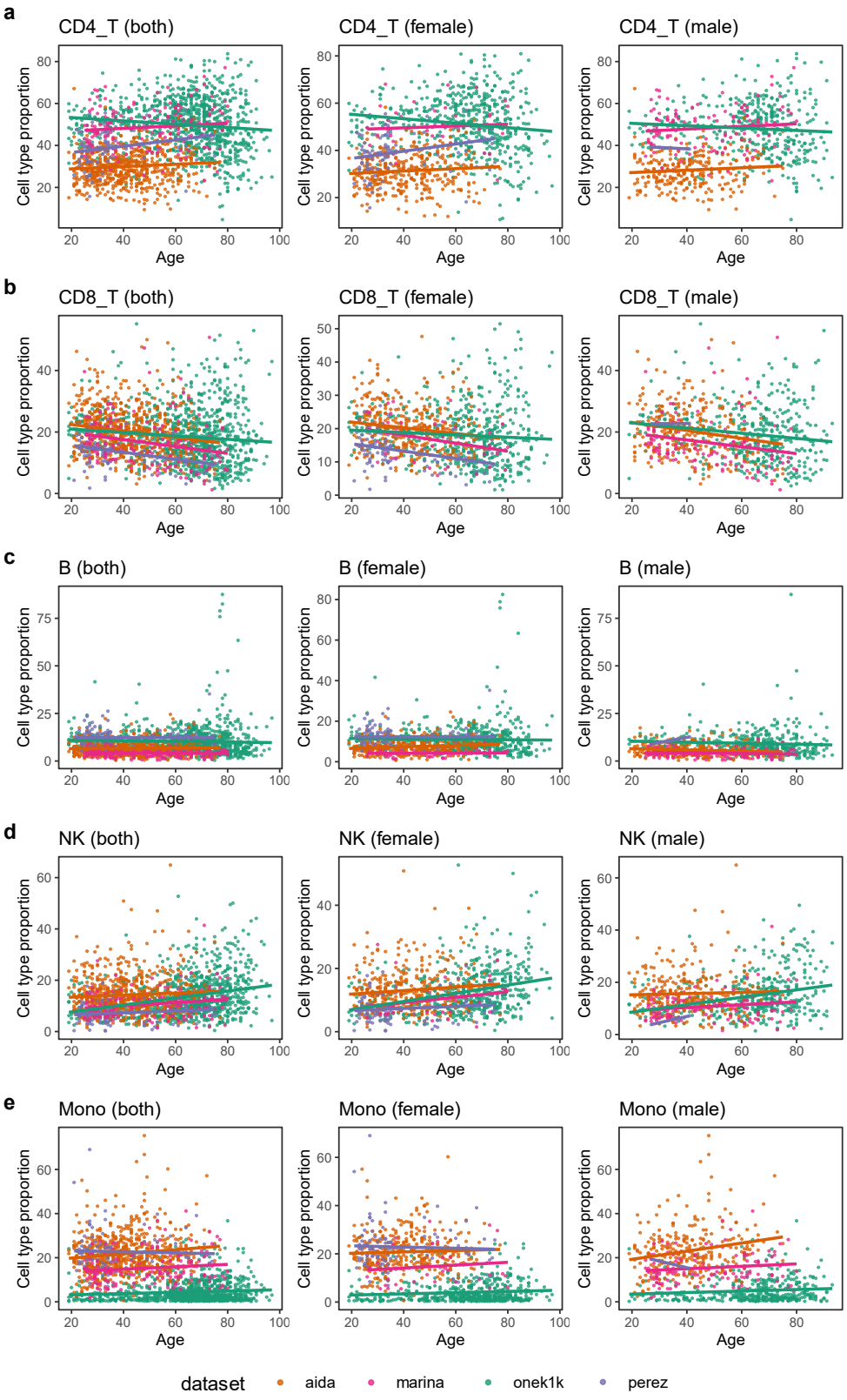

Supplementary Fig. 3: Age-associated changes in major cell type proportions across the four datasets. a-e, Cell type proportions plotted against age for CD4 T cells (**a**), CD8 T cells (**b**), B cells (**c**), NK cells (**d**), and monocytes (**e**). Data are shown separately for all samples (n = 1,828), female samples (n = 1,021), and male samples (n = 807). Points and regression lines are colored by each dataset.

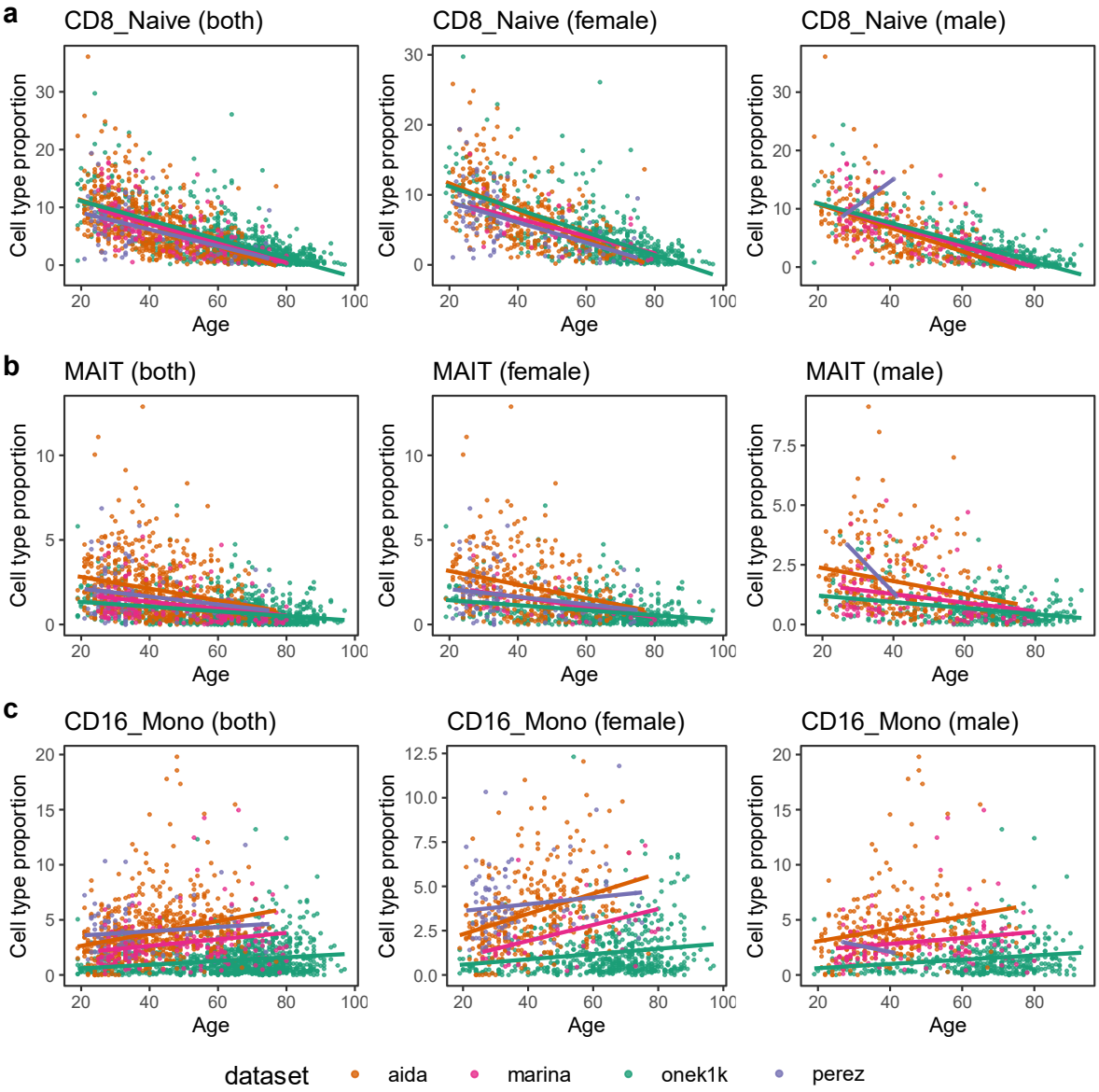

Supplementary Fig. 4: Age-associated changes in detailed cell subtype proportions across the four datasets. a-c, Cell type proportions plotted against age for CD8 Naïve T cells (**a**), MAIT cells (**b**), and CD16 monocytes (**c**). Data are shown separately for all samples (n = 1,828), female samples (n = 1,021), and male samples (n = 807). Points and regression lines are colored by each dataset.

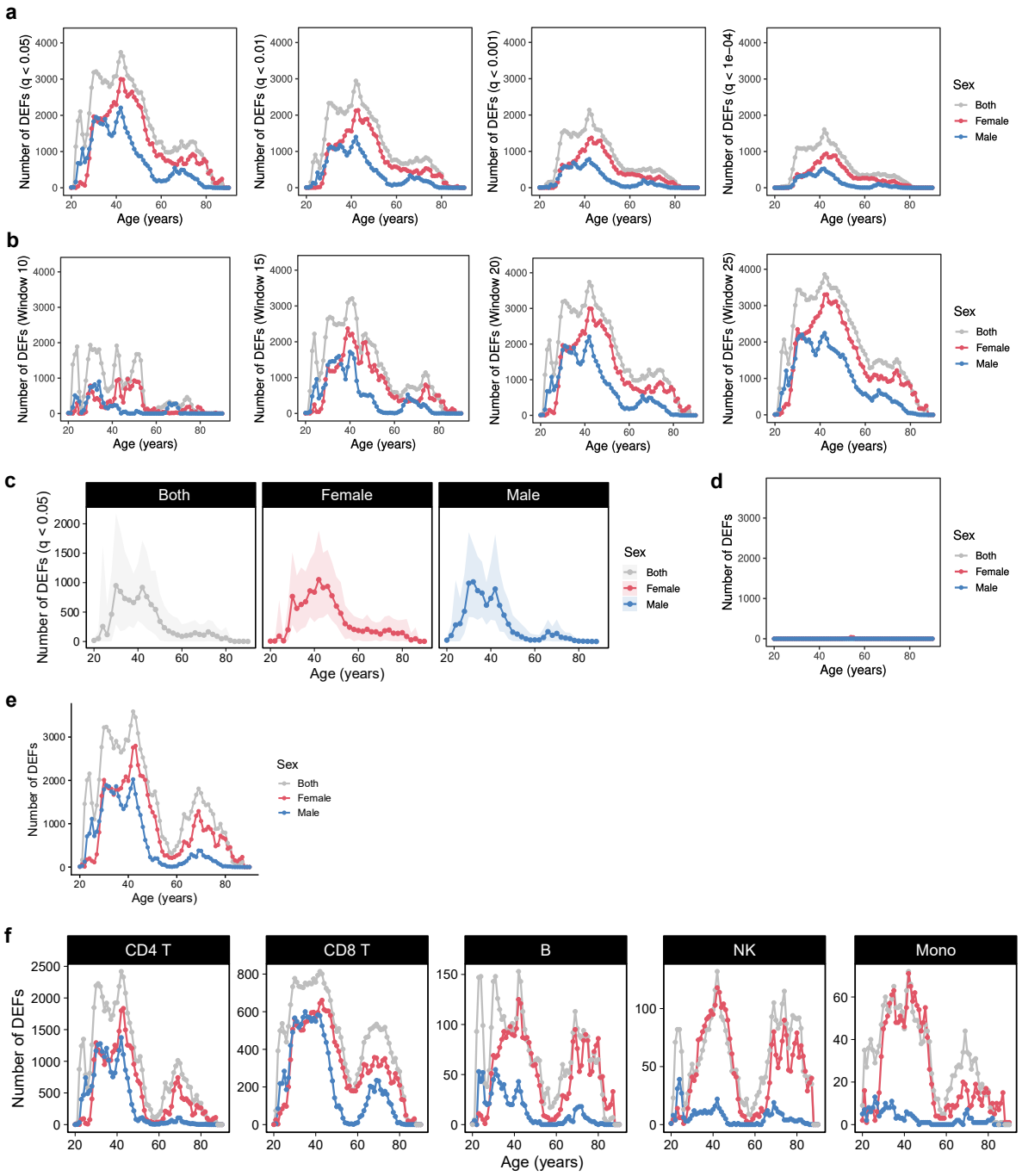

Supplementary Fig. 5: Robustness and validation of differential expression-sliding window analysis (DE-SWAN) analysis. a-d, Number of differentially expressed features (DEFs; q < 0.05 unless otherwise stated) across age identified by DE-SWAN using different q-value cutoffs (**a**), different window sizes (**b**), 100 random downsampling iterations, each using 200 samples (**c**), and randomly shuffled ages (**d**). **e-f**, Number of DEFs (q < 0.05) across age identified by DE-SWAN analysis with limma's batch effect correction, shown for all major peripheral blood mononuclear cell (PBMC) types combined (**e**) and for each cell type separately (**f**).

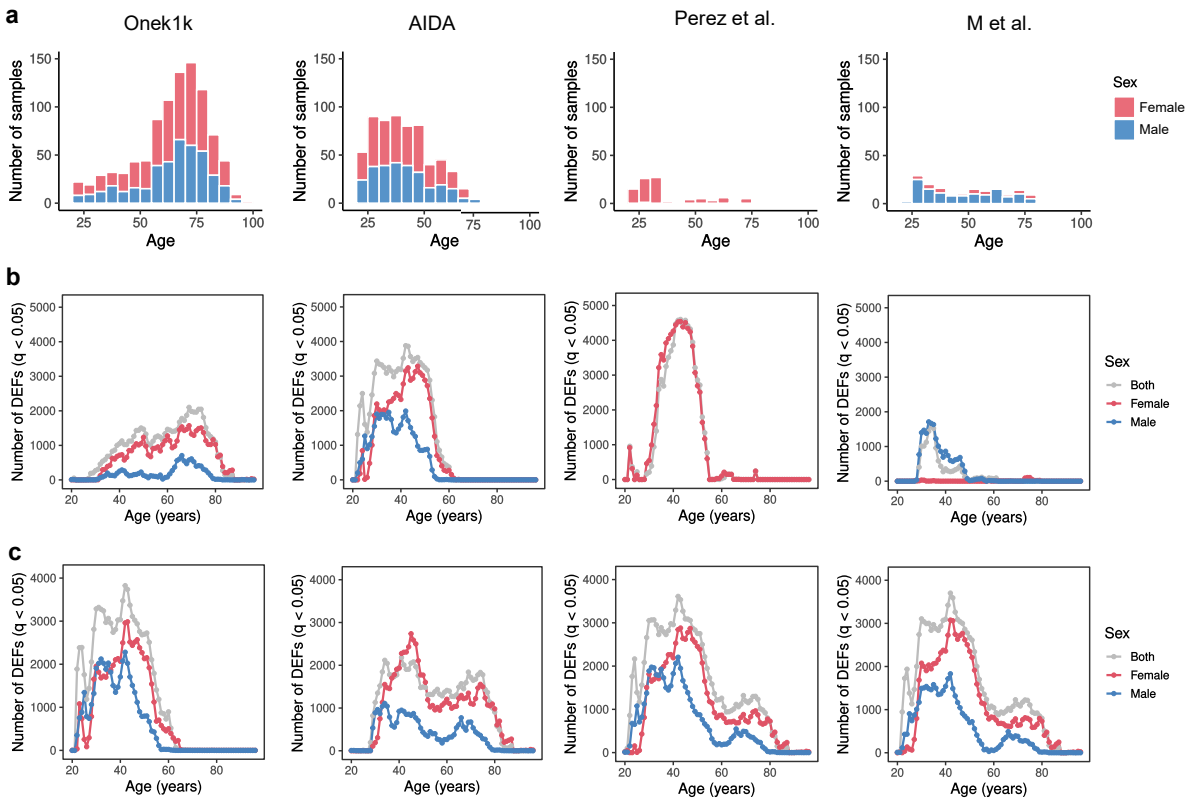

Supplementary Fig. 6: Individual dataset differential expression-sliding window analysis (DE-SWAN) results. a, Age and sex distribution in individual datasets (n = 949, 622, 88, 317). **b**-**c**, Number of differentially expressed features (DEFs, q < 0.05) across age identified by DE-SWAN when using each dataset individually (**b**) or using leave-one-out analysis (**c**).

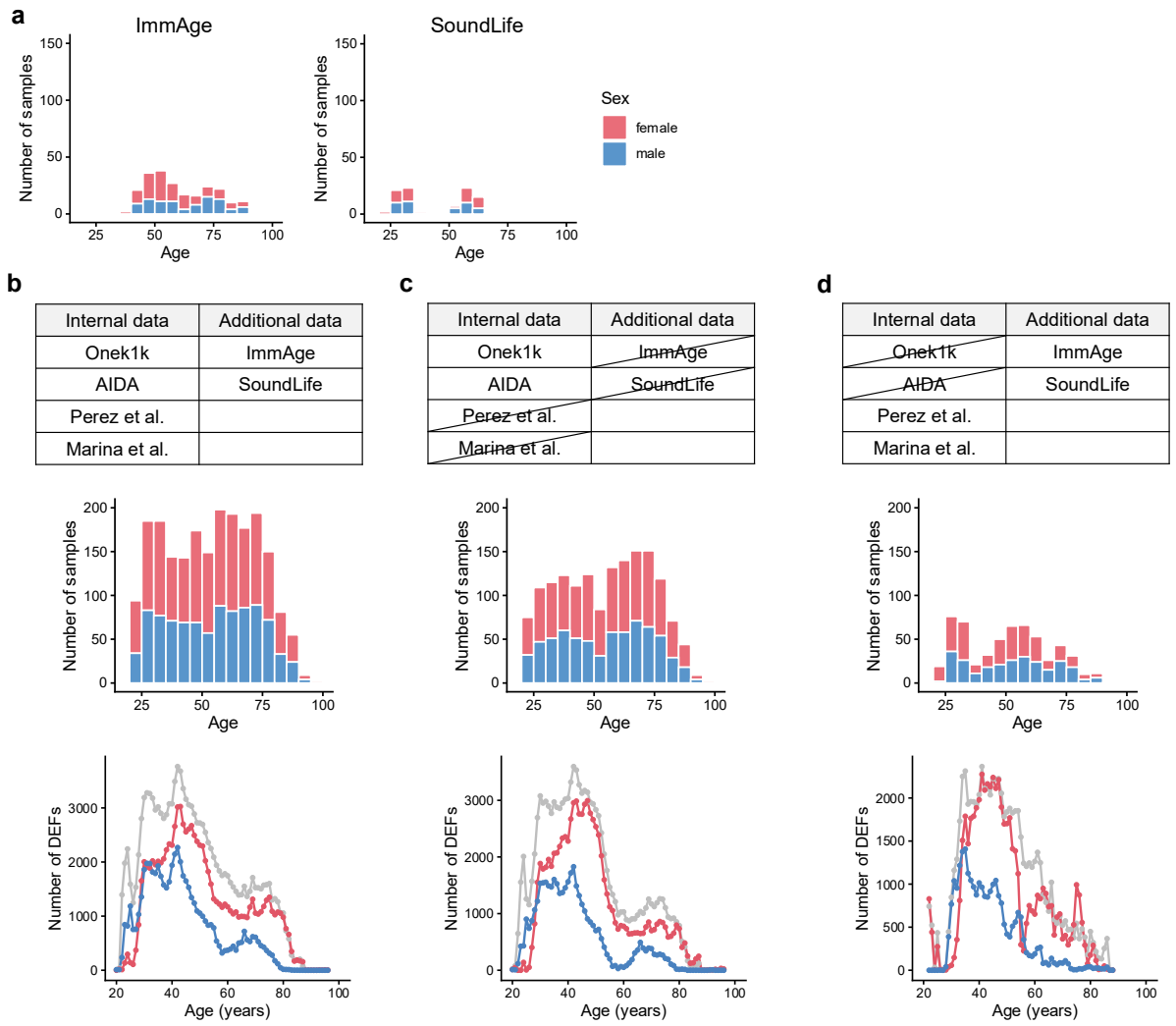

Supplementary Fig. 7: Reproducibility of DE-SWAN peaks using additional PBMC scRNA-seq datasets. a, Age and sex distribution of the ImmAge (n = 224) and SoundLife (n = 92) datasets, which were used as additional human peripheral blood mononuclear cells (PBMC) single-cell RNA sequencing (scRNA-seq) data for validation. **b-d**, Summary of included datasets, their age and sex distributions, and differential expression-sliding window analysis (DE-SWAN) results under different dataset combinations: all internal and additional datasets (**b**); Onek1k and AIDA datasets only (**c**); and Perez et al., Marina et al., and additional datasets (**d**).

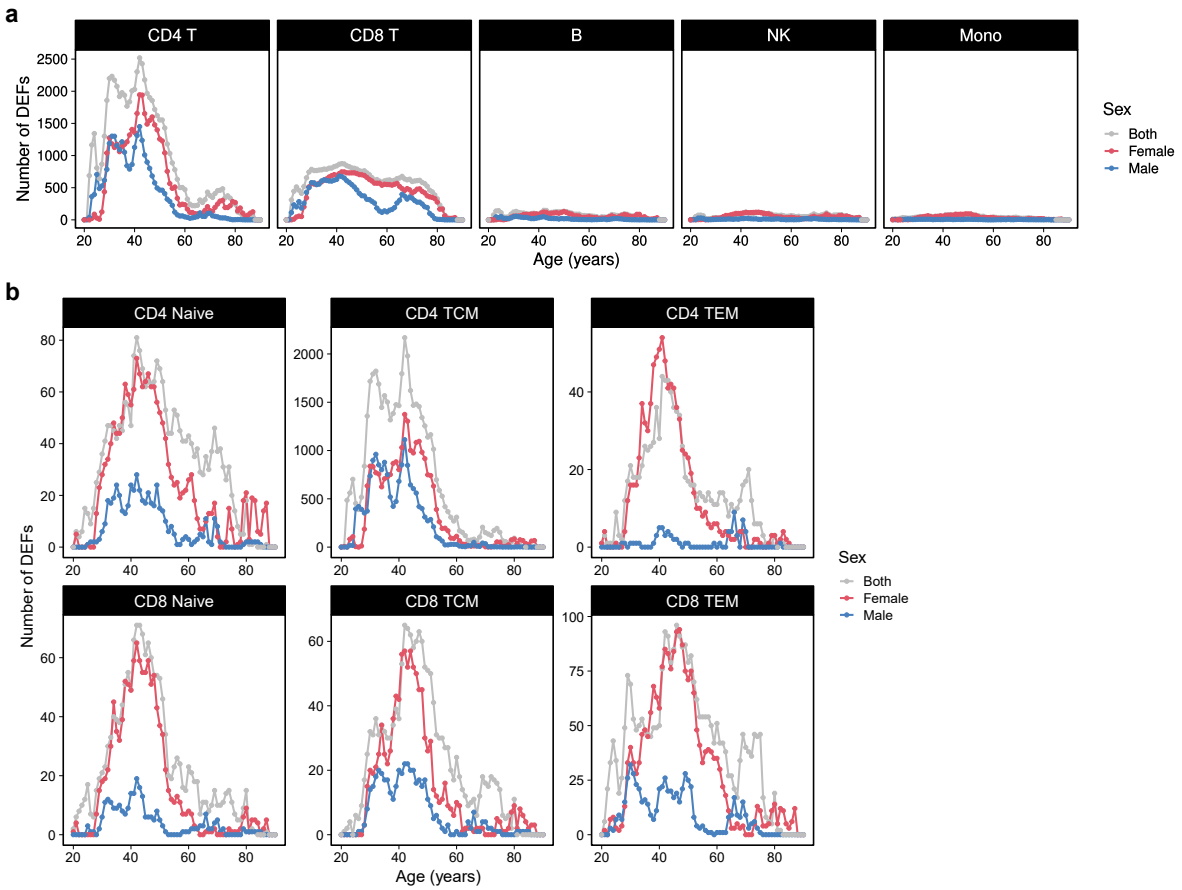

Supplementary Fig. 8: DE-SWAN results at the cell type level. a, Number of differentially expressed features (DEFs, q < 0.05) across age for each major cell types (level 1), with a consistent y-axis. **b**, Number of DEFs (q < 0.05) across age for detailed cell types (level 2) within the T cell compartment.

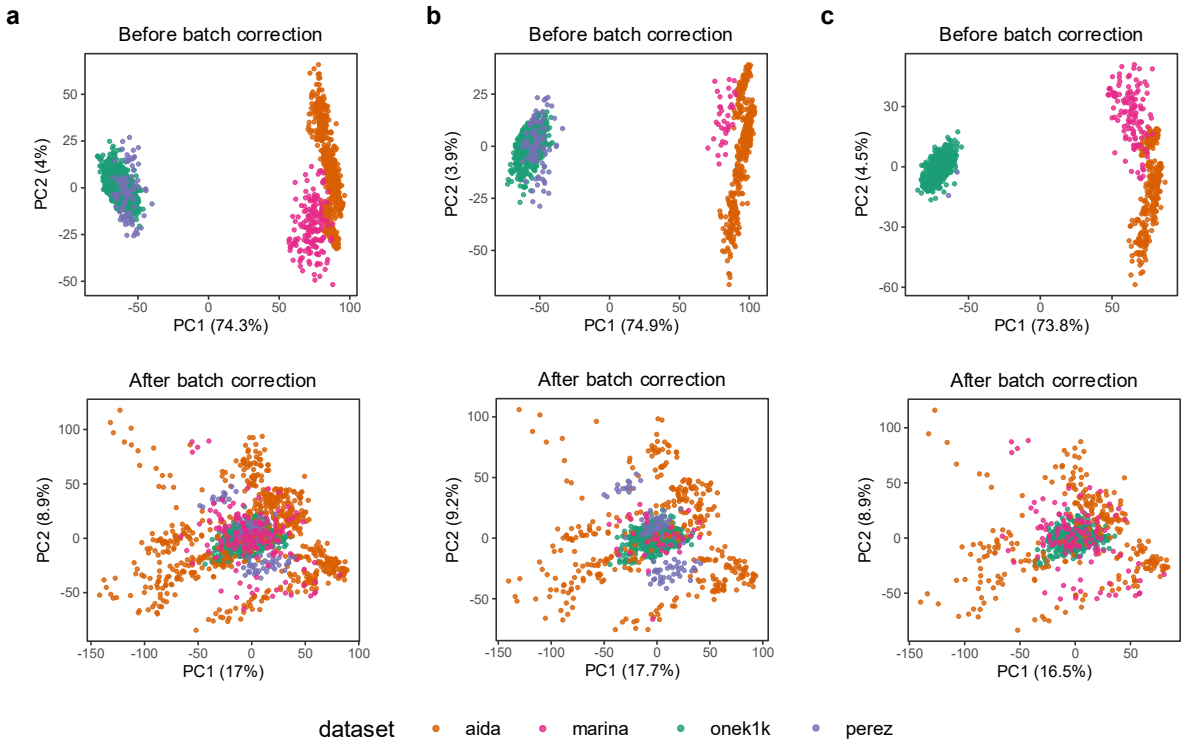

Supplementary Fig. 9: Batch effect correction for pseudobulk expression matrices. a-c, Principal component analysis (PCA) plots before and after batch effect correction for both-sex (n = 1,828) (**a**), female (n = 1,021) (**b**), and male (n = 807) (**c**) pseudobulk expression matrices.

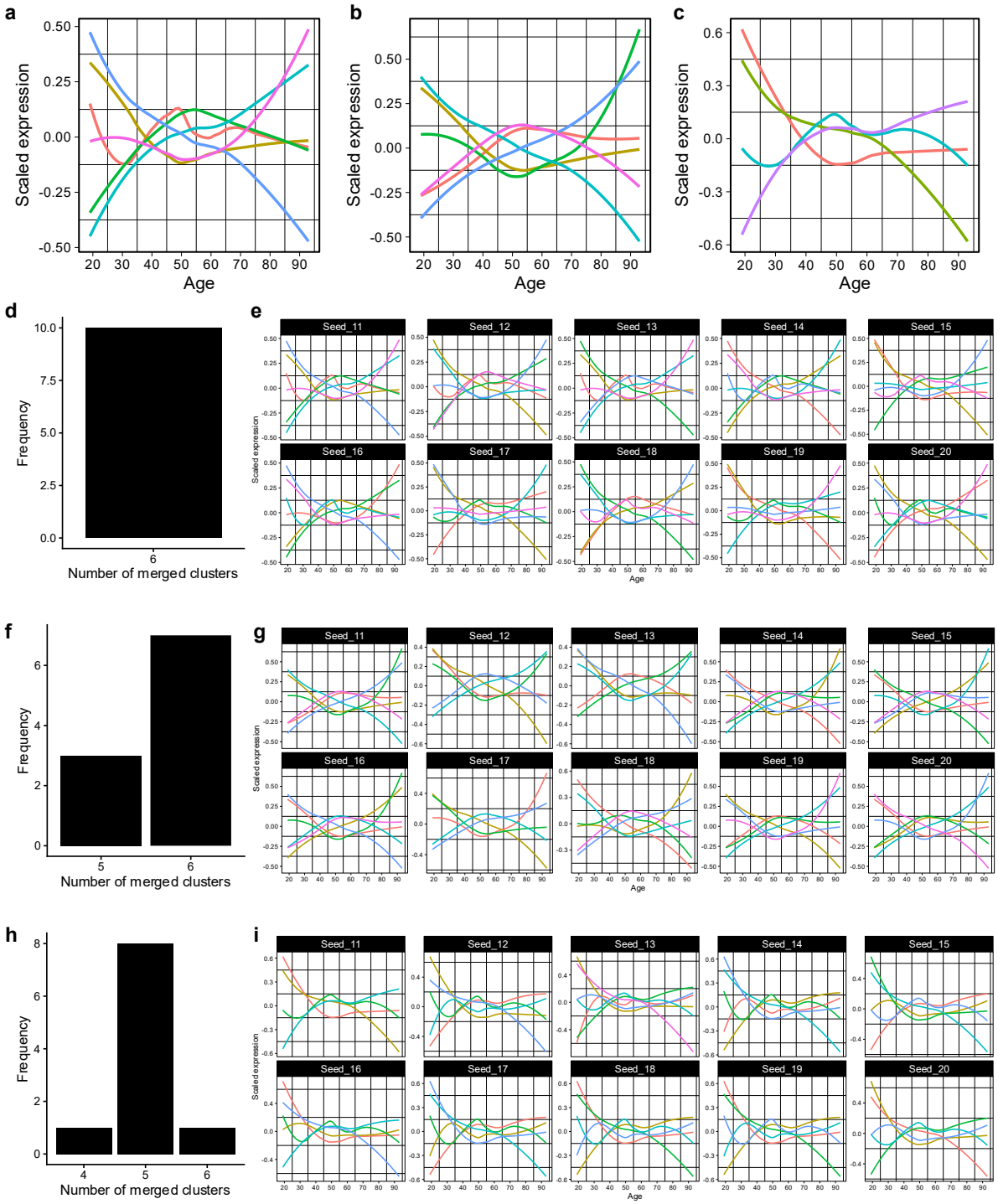

Supplementary Fig. 10: Reproducibility of SAF trajectory clustering. a-c, Final cluster trajectories for both-sex (**a**), female (**b**), and male (**c**) sex-aware aging features (SAFs). **d-i**, Number of clusters and cluster trajectories across 10 independent clustering runs with different random seeds for both-sex (**d-e**), female (**f-g**), and male (**h-i**) SAFs.

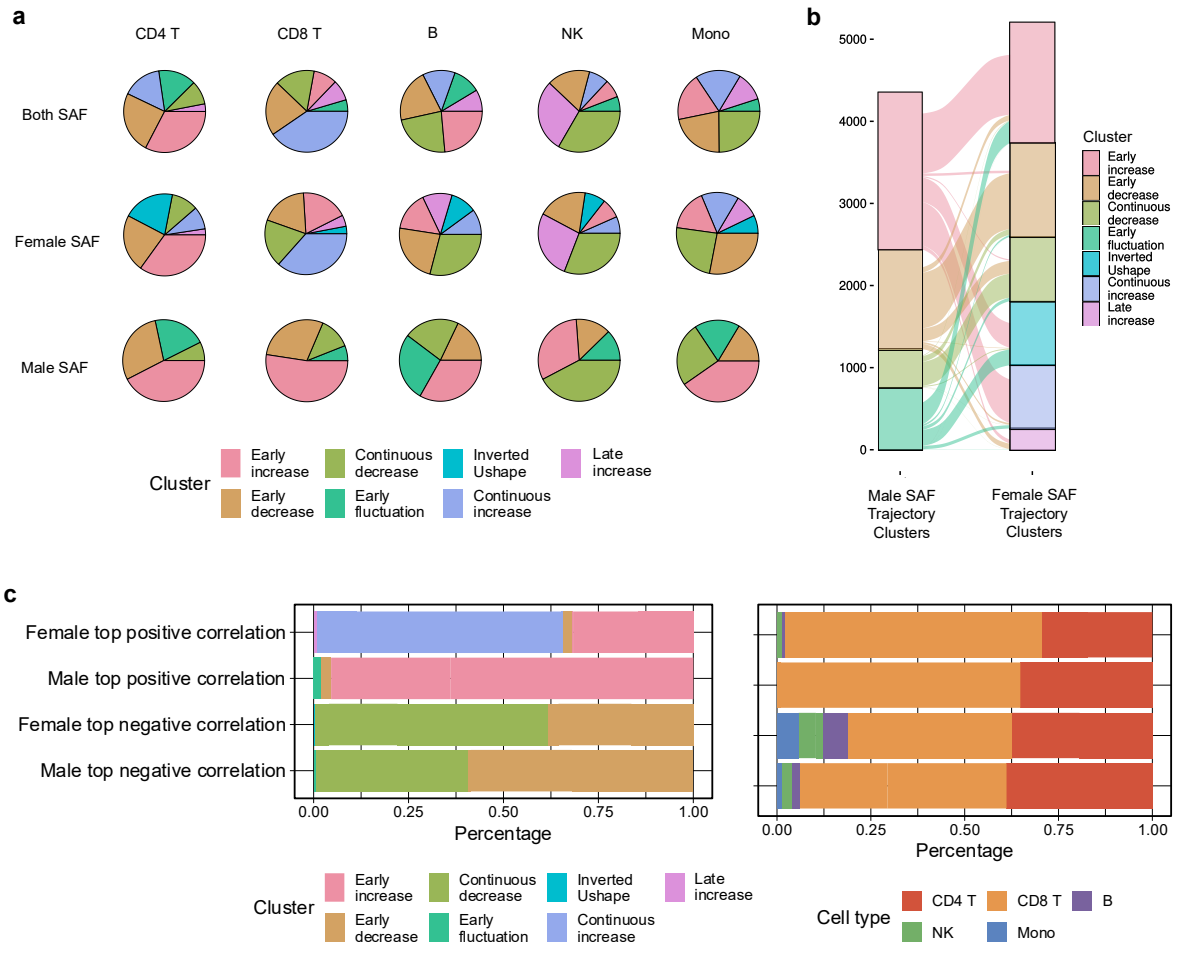

Supplementary Fig. 11: Cell type composition and correlation profiles of trajectory clusters. a, Cell type composition and distribution across temporal kinetics clusters for both-sex, female, and male sex-aware aging features (SAFs). **b**, Assignment flow chart of features across male and female SAF trajectory clusters. **c**, Features with top positive and negative Spearman correlation in females and males (top percentile), colored by cluster assignment and cell type.

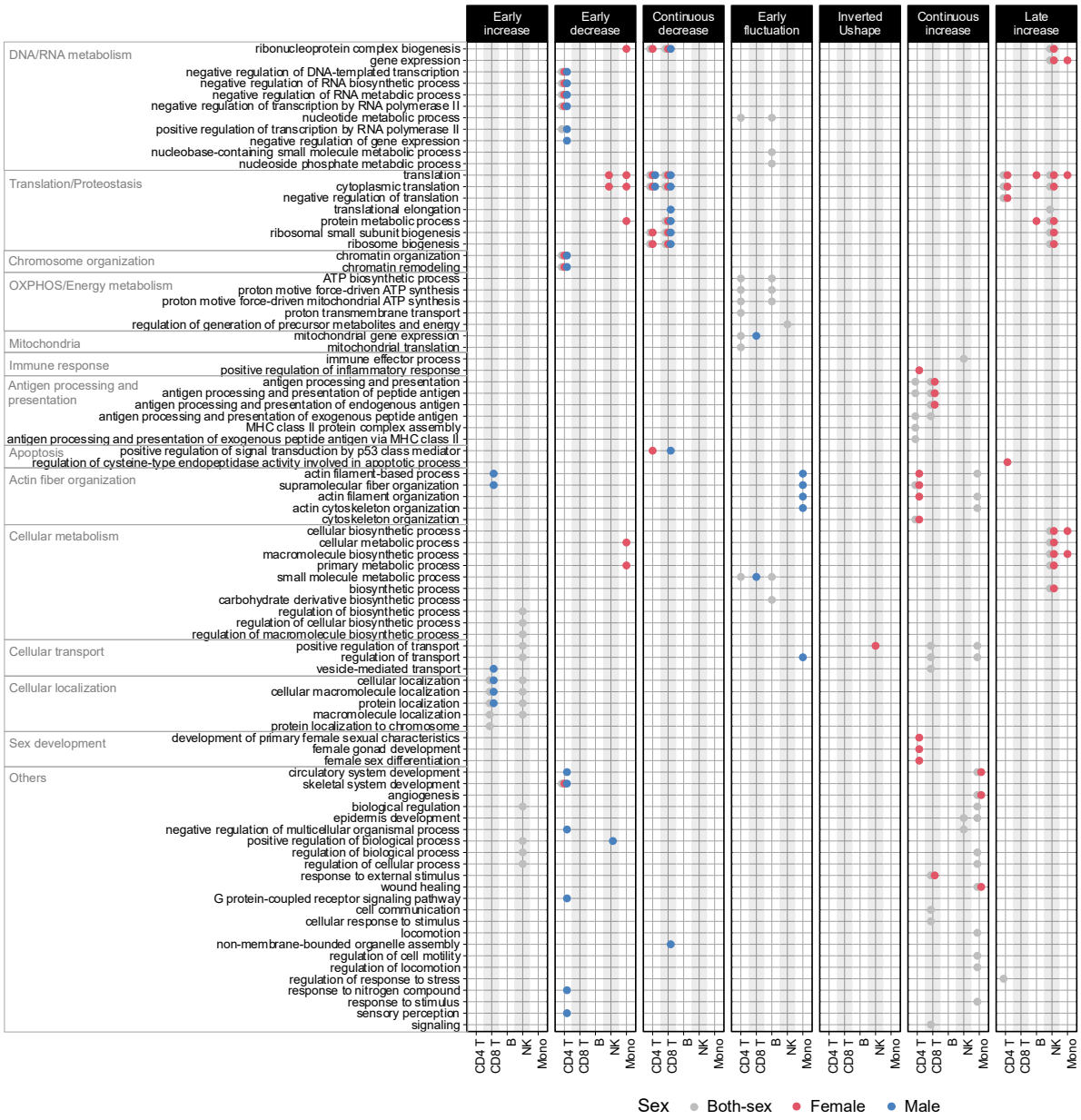

Supplementary Fig. 12: Functional annotation of sex-stratified trajectory clusters. Pathway enrichment results of Gene Ontology Biological Process (GOBP) terms ($q < 0.1$) separated by sex and cell type, ordered by functional module based on manual annotation.

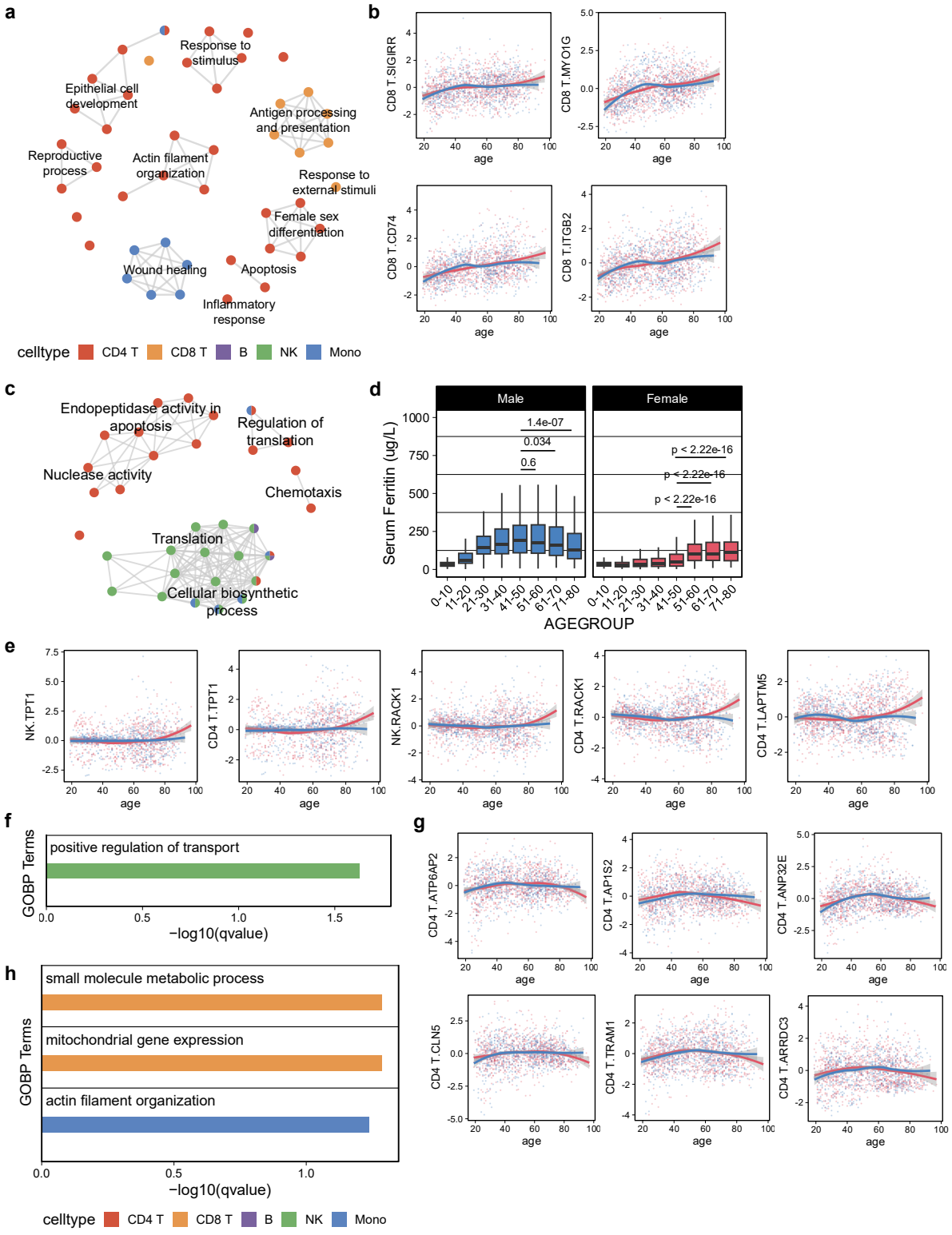

Supplementary Fig. 13: Functional characterization of sex-specific trajectory clusters. **a**, Network visualization of Gene Ontology Biological Process (GOBP) pathway enrichment results (q < 0.1) of the female continuous increase cluster. Nodes represent pathways colored by cell types showing significant enrichment. Edges connect pathways with Jaccard index >0.25. **b**, Scaled pseudobulk expression trajectories of representative features from the female continuous increase features across age, colored by sex. **c**, Network visualization of GOBP pathway enrichment results (q < 0.1) of the female late increase cluster. Nodes represent pathways colored by cell types showing significant enrichment. Edges connect

pathways with Jaccard index >0.25. **d**, Serum ferritin levels across 10-year age groups by sex from the National Health and Nutrition Examination Survey (NHANES) 2017-2018 dataset (n = 3,378 females, 3,211 males). Data are presented in box plots as median (center line), interquartile range (IQR; box), and whiskers extending to 1.5 × IQR, and p-values were calculated using two-sided Mann-Whitney U test. **e**, Scaled pseudobulk expression trajectories of representative late increase features across age, colored by sex. **f**, Top GOBP term from pathway enrichment analysis of the female inverted U-shape cluster. **g**, Scaled pseudobulk expression trajectories of representative inverted U-shape features across age, colored by sex. **h**, Top GOBP terms from pathway enrichment analysis of the male early fluctuation cluster. Shaded area represents the 95% confidence interval of the fitted LOESS regression line in **b**, **e**, **g**.

Supplementary Fig. 14: Epigenetic analysis for mechanisms underlying sex-specific trajectories. a, Age and sex distribution in the DNA methylation array dataset (GSE87571; n = 729). **b**, Chromosomal positions of two chr6p21 differentially methylated regions (DMRs) from young vs. middle-aged and young vs. old comparisons. **c**, **e**, Mean beta values grouped by age group and stratified by sex for each CpG in the corresponding DMRs. **d**, **f**, Mean beta values grouped by age group and stratified by sex for all CpGs in the corresponding DMRs (n = 153,116,119 (female); n = 116,115,110 (male)). Data are presented in box plots as median (center line), interquartile range (IQR; box), and whiskers extending to 1.5 × IQR, and p-values were calculated using two-sided Mann-Whitney U test in **d**, **f**.

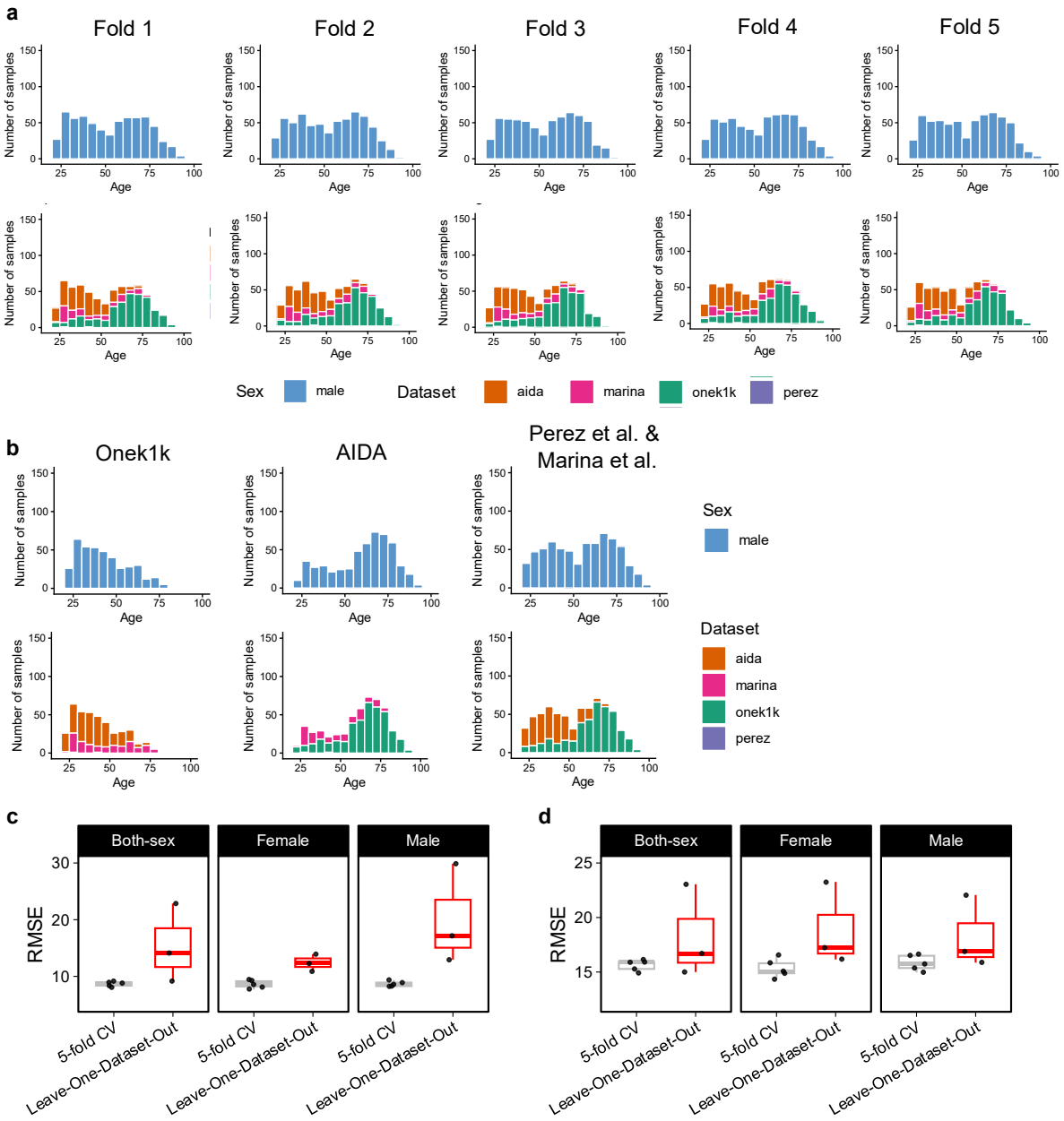

Supplementary Fig. 15: Comparison of 5-fold cross-validation (CV) and leave-one-dataset-out (LODO) validation approaches as a sensitivity analysis. a, Age distribution and dataset composition of the five training folds used to build the male MLP models. **b**, Age distribution and dataset composition of the LODO training sets when each dataset was held out. **c-d**, Root mean squared error (RMSE) of sex-combined and sex-stratified models trained using 5-fold CV or LODO, evaluated on the internal test set (**c**) and external test set (**d**).

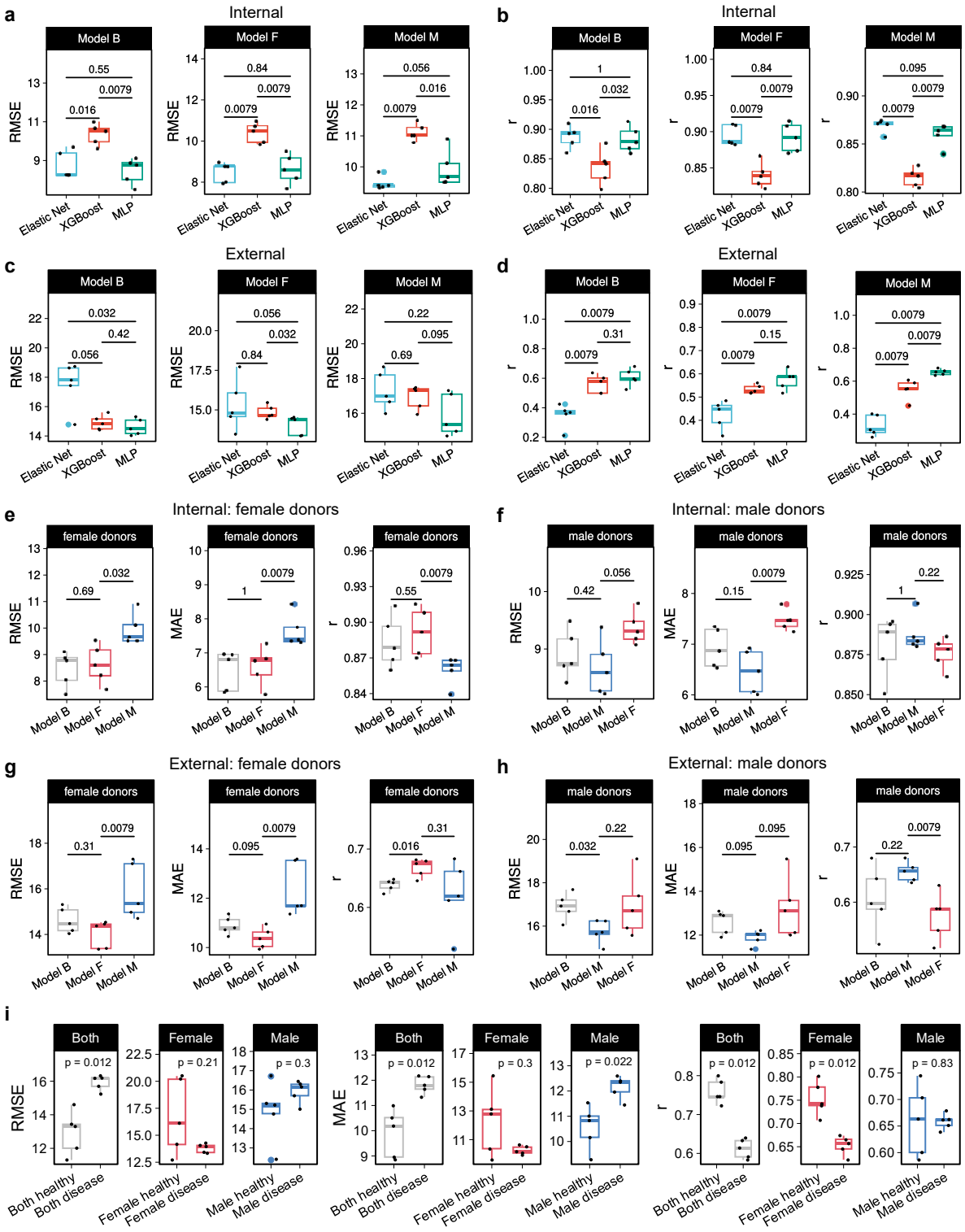

Supplementary Fig. 16: Model performance comparison and sex-stratified clock validation. a, **b**, Root mean squared error (RMSE) (**a**) and Pearson *r* (**b**) comparison among Elastic Net, Extreme Gradient Boosting (XGBoost), and multilayer perceptron (MLP) across 5 cross-validation folds in internal test sets. **c**, **d**, RMSE (**c**) and Pearson *r* (**d**) comparison among Elastic Net, XGBoost, and MLP across 5 cross-validation folds in external validation sets (healthy and disease cohorts combined). **e**, **f**, Performance metrics comparison of sex-combined versus sex-specific models in female (**e**) and male donors (**f**) in internal test sets. **g**, **h**, Performance metrics comparison of sex-combined versus sex-specific models in female (**e**)

and male donors (**f**) in external validation sets. **i**, RMSE, mean absolute error (MAE), and Pearson *r* comparison of MLP models on healthy versus disease cohorts. Data are presented in box plots as median (center line), interquartile range (IQR; box), and whiskers extending to 1.5 × IQR. P-values were calculated using two-sided Mann-Whitney U test.

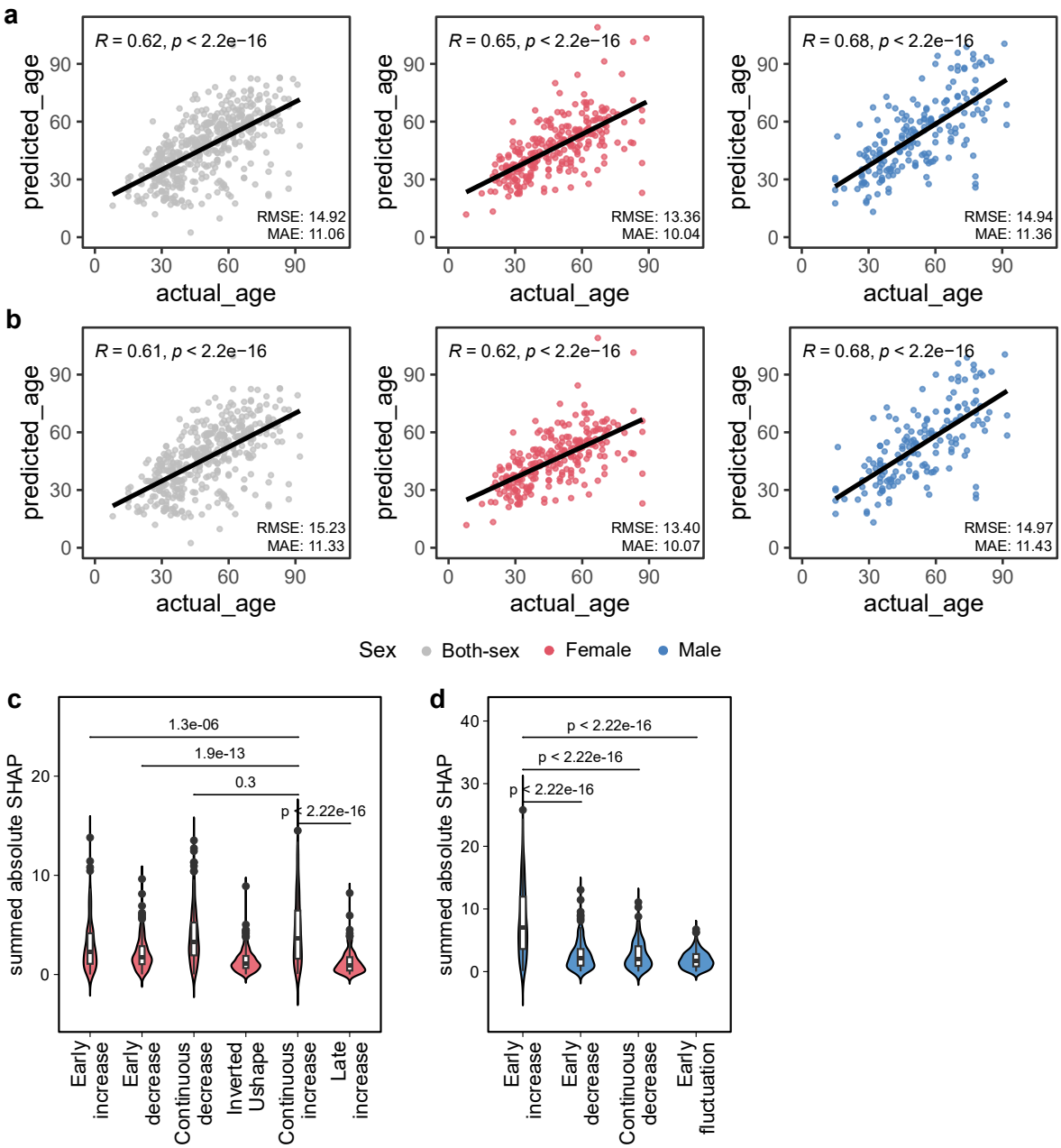

Supplementary Fig. 17: Age prediction performance and SHAP analysis of final sex-stratified biological aging clocks. a, **b**, Chronological age versus predicted age by sex-combined and sex-stratified models on full external validation set (healthy and disease cohorts combined) (**a**) and disease cohort only (**b**), with Pearson correlation coefficients, root mean squared error (RMSE), and mean absolute error (MAE) indicated in each panel. P-values were calculated using two-sided Student's t-test. **c**, **d**, Summed absolute SHapley Additive exPlanations (SHAP) values by trajectory cluster in female (**c**) and male donors (**d**). Data are presented in box plots as median (center line), interquartile range (IQR; box), and whiskers extending to 1.5 × IQR, and p-values were calculated using two-sided Mann-Whitney U test in **c**-**d**.

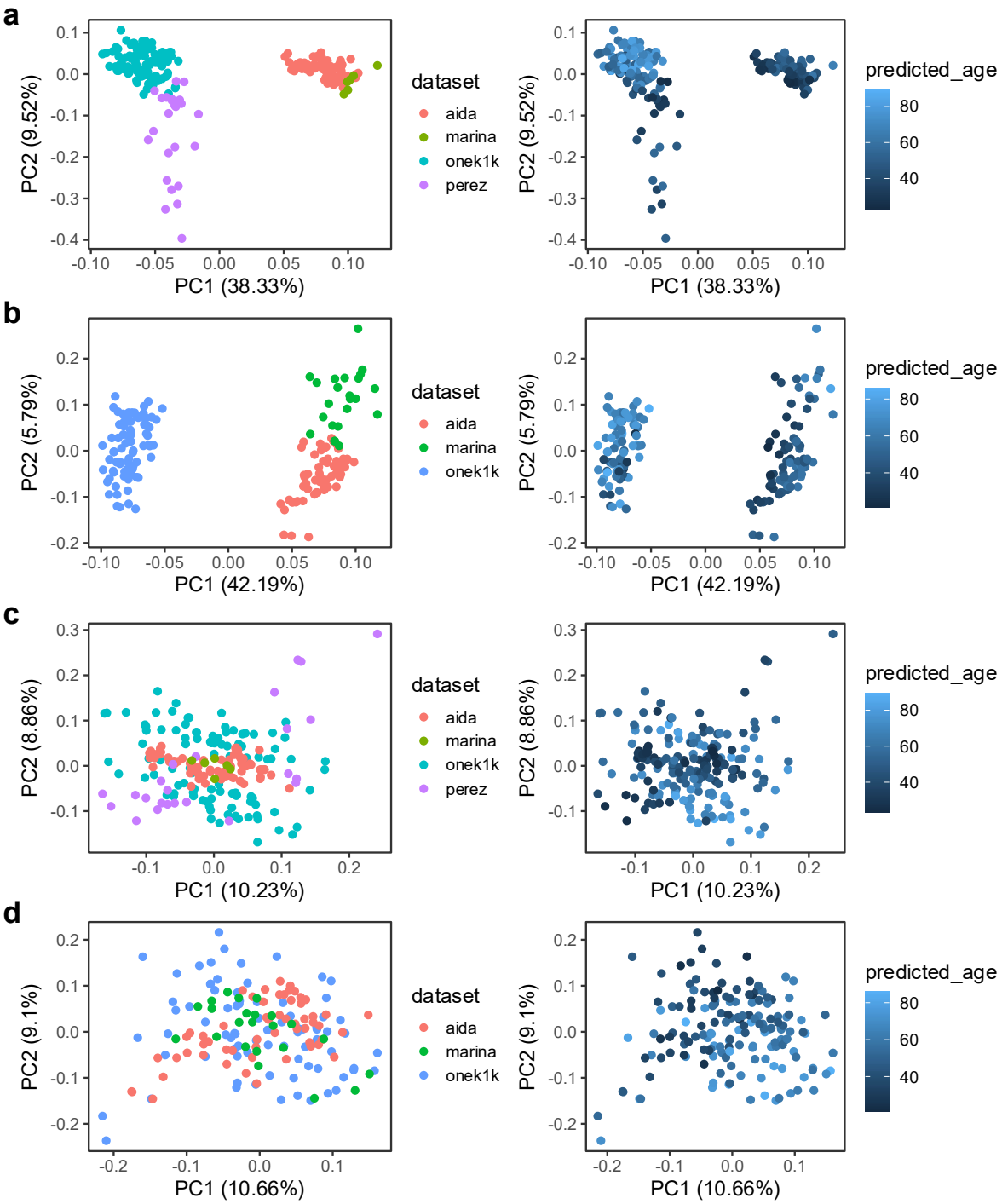

Supplementary Fig. 18: SHAP value correction for dataset batch effects. a, **b**, Principal component analysis (PCA) of raw Shapely Additive exPlanations (SHAP) values colored by dataset identity and chronological age for female donors (female-specific clock) (**a**) and male donors (male-specific clock) (**b**). **c**, **d**, PCA of corrected SHAP values colored by dataset identity and chronological age for female donors (female-specific clock) (**c**) and male donors (male-specific clock) (**d**).

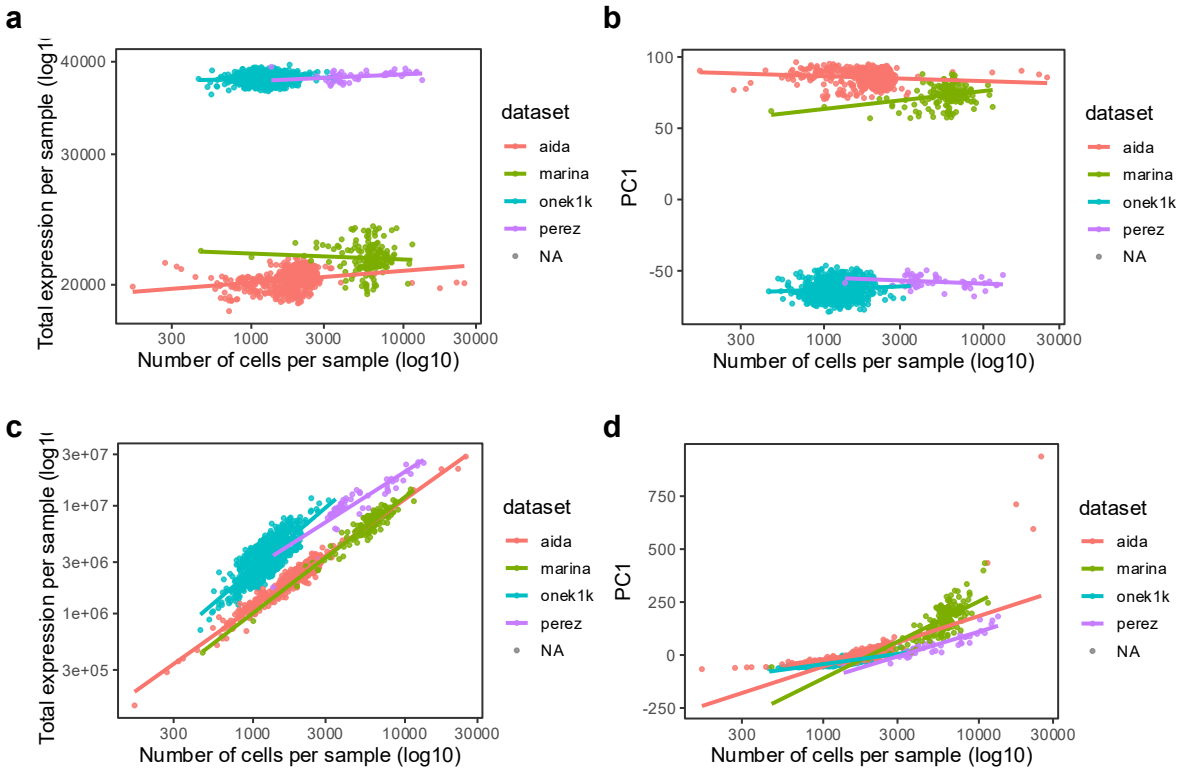

Supplementary Fig. 19: Comparison of pseudobulk aggregation strategies. a-b, Correlation between cell count per sample and total pseudobulk expression (**a**) or principal component 1 (PC1) of final pseudobulk matrix (**b**) when using average expression per cell. **b-c**, Correlation between cell count per sample and total pseudobulk expression (**c**) or PC1 of final pseudobulk matrix (**d**) when using summed counts.

Supplementary Table 1. Genes at chromosome 11q13 in early fluctuation CD4 T cell features.

Gene	Description	Chromosome	Start	End
OTUB1	OTU Deubiquitinase, Ubiquitin Aldehyde Binding 1	chr11	63985853	64001811
STIP1	Stress Induced Phosphoprotein 1	chr11	64185272	64204548
FERMT3	FERM Domain Containing Kindlin 3	chr11	64205920	64223896
NUDT22	Nudix Hydrolase 22	chr11	64225941	64230686
TRMT112	TRNA Methyltransferase Activator Subunit 11-2	chr11	64316460	64318596
PRDX5	Peroxiredoxin 5	chr11	64318041	64321822
ARL2	ARF Like GTPase 2	chr11	65014144	65024328
DPF2	Double PHD Fingers 2	chr11	65333821	65354262
SCYL1	SCY1 Like Pseudokinase 1	chr11	65526072	65538711
LTBP3	Latent Transforming Growth Factor Beta Binding Protein 3	chr11	65538559	65558930
ZNRD2	Zinc Ribbon Domain Containing 2	chr11	65570459	65573942
FIBP	FGF1 Intracellular Binding Protein	chr11	65883740	65888531
CCDC85B	Coiled-Coil Domain Containing 85B	chr11	65890673	65891635
DRAP1	DR1 Associated Protein 1	chr11	65919274	65921563
RAB1B	RAB1B, Member RAS Oncogene Family	chr11	66268590	66277492
YIF1A	Yip1 Interacting Factor Homolog A, Membrane Trafficking Protein	chr11	66284572	66289184
MRPL11	Mitochondrial Ribosomal Protein L11	chr11	66435075	66466738
POLD4	DNA Polymerase Delta 4, Accessory Subunit	chr11	67350765	67356972
PPP1CA	Protein Phosphatase 1 Catalytic Subunit Alpha	chr11	67398179	67421183
TBC1D10C	TBC1 Domain Family Member 10C	chr11	67398454	67410092
TMEM134	Transmembrane Protein 134	chr11	67461710	67469288
CDK2AP2	Cyclin Dependent Kinase 2 Associated Protein 2	chr11	67506490	67508701
NDUFS8	NADH:Ubiquinone Oxidoreductase Core Subunit S8	chr11	68030617	68036647
KMT5B	Lysine Methyltransferase 5B	chr11	68154863	68213852
COA4	Cytochrome C Oxidase Assembly Factor 4 Homolog	chr11	73869846	73876982
SPCS2	Signal Peptidase Complex Subunit 2	chr11	74949259	74979033

Supplementary Table 2. Autosomal DMRs with significant age-sex interaction.

comparison	chr	start	end	width	strand	No cpgs	Min smoothed fdr	Stouffer	HMFDR	Fisher	maxdiff	meandiff	Overlapping genes
Young vs. Middle-aged	chr6	31691354	31692375	1022	*	27	2.89E-21	7.69E-27	0.0018	2.92E-24	-0.035	-0.018	C6orf25
Young vs. Middle-aged	chr12	11002403	11002609	207	*	3	1.57E-14	2.42E-16	8.14E-10	2.27E-16	-0.15	-0.077	PRR4
Young vs. Old	chr19	11289087	11289376	290	*	8	3.05E-19	7.88E-16	6.76E-09	4.03E-20	-0.043	-0.018	KANK2
Young vs. Old	chr12	11002071	11002609	539	*	5	1.80E-18	2.06E-16	5.51E-10	1.16E-18	-0.16	-0.045	PRR4
Young vs. Old	chr6	32191210	32191895	686	*	6	6.90E-17	2.35E-13	5.85E-07	7.31E-14	-0.044	-0.030	NOTCH4
Young vs. Old	chr17	79792334	79793439	1106	*	12	1.16E-14	1.04E-17	0.00015	1.86E-16	-0.033	-0.017	PPP1R27
Young vs. Old	chr5	92956474	92957098	625	*	9	3.99E-14	9.14E-16	9.15E-06	1.00E-15	0.020	0.0076	FAM172A, MIR2277
Young vs. Old	chr17	57915665	57915773	109	*	4	1.09E-13	5.61E-16	3.72E-07	1.72E-15	-0.085	-0.063	VMP1
Young vs. Old	chr6	33287809	33288372	564	*	9	6.66E-13	1.90E-12	0.00012	2.95E-14	-0.042	-0.014	DAXX
Young vs. Old	chr11	67070967	67071322	356	*	3	5.26E-10	2.64E-05	0.00056	2.56E-05	-0.042	-0.025	SSH3
Young vs. Old	chr6	31698722	31698899	178	*	3	6.71E-10	1.69E-05	0.0013	4.02E-05	-0.021	-0.017	CLIC1
Young vs. Old	chr19	16830613	16830859	247	*	5	9.11E-10	3.22E-10	4.99E-05	1.00E-11	-0.054	-0.037	NWD1